Journal of Structural Biology 217 (2025) 108206

Contents lists available at ScienceDirect

Journal of Structural Biology

journal homepage: www.elsevier.com/locate/yjsbi

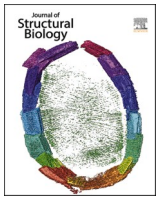

Research Article

Untangling the effects of flexibility and the AWI in cryoEM sample preparation: A case study using KtrA

Isobel Jackson Hirst [a], Wesley Tien Chiang [b], Nien-Jen Hu [b], Charlotte A. Scarff [c], Rebecca F. Thompson [d,1], Michele C. Darrow [e,*], Stephen P. Muench [a,*]

[a] School of Biomedical Sciences, Faculty of Biological Sciences & Astbury Centre for Structural and Molecular Biology, University of Leeds, Leeds, UK
[b] Graduate Institute of Biochemistry, National Chung Hsing University, Taichung City 402202, Taiwan
[c] Discovery and Translational Science Department, Leeds Institute of Cardiovascular and Metabolic Medicine, School of Medicine, Faculty of Medicine & Health & Astbury Centre for Structural and Molecular Biology, University of Leeds, Leeds, UK
[d] Previous address: School of Molecular and Cellular Biology, Faculty of Biological Sciences & Astbury Centre for Structural and Molecular Biology, University of Leeds, Leeds, UK
[e] The Rosalind Franklin Institute, Harwell Campus, Didcot, UK

ARTICLE INFO

Keywords:
Air-water interface
Cryo-electron microscopy
Flexibility
KtrA
Sample preparation

ABSTRACT

Single particle cryo-electron microscopy (cryoEM) is a powerful tool for elucidating the structures of biological macromolecules without requiring crystallisation or fixation. However, certain barriers to obtaining high-resolution structures persist, particularly during grid preparation when samples are in a thin liquid film. At this stage, extensive exposure to the air–water interface (AWI) can lead to subunit dissociation, denaturation, and preferred orientation of particles. Another obstacle to high-resolution cryoEM is molecular flexibility, which introduces heterogeneity in the dataset, weakening the signal during image processing. This study explores the effects of AWI interactions and molecular flexibility on the cryoEM density maps of KtrA, the soluble regulatory subunit of the potassium transporter KtrAB from *Bacillus subtilis*. From grids prepared using a standard blotting technique, we observed a lack of density in the C-lobe domains and preferred orientation. Modifications such as reducing AWI exposure through faster vitrification times (6 s vs ≤100 ms) notably improved C-lobe density. Moreover, the addition of cyclic di-AMP, which binds to the C-lobes, combined with a 100 ms plunge time, further enhanced C-lobe density and eliminated preferred orientation. These findings demonstrate that both AWI interactions and flexibility had to be addressed to obtain density for the C-lobe domains of KtrA. This study underscores the ongoing complexities in achieving high-resolution cryoEM for many samples.

1. Introduction

It is now possible to use single particle cryo electron microscopy (cryoEM) to achieve high resolution (<2.5 Å) structures of a wide variety of proteins from small (<100 kDa) membrane proteins to mega Dalton complexes (Mobbs, 2021; Han, 2023). Despite the versatility and power of cryoEM, there remains many samples for which it is not possible to solve a high-resolution structure, including samples that one would expect to be straight forward (Weissenberger et al., 2021). There is a myriad of factors that can cause barriers to high-resolution cryoEM, including protein degradation, flexibility, complex dissociation, preferred orientation and poor particle distribution on the grid (Glaeser, 2021; Punjani et al., 2020; Yadav and Vinothkumar, 2024).

Over the past decade, an increasing amount of attention has been paid to the consequences of behaviour of protein particles at the extensive air–water interface (AWI) that is required on the grid prior to vitrification to ensure suitable ice thickness (Yadav and Vinothkumar, 2024; Chen, 2022; D'Imprima and Kuhlbrandt, 2021; Glaeser, 2018; Glaeser and Han, 2017; Klebl, 2020; Klebl, 2022; Levitz, 2022; Noble, 2018). These studies and others have shown that taking steps to reduce or moderate AWI interactions can reduce preferred orientation and protein complex dissociation or denaturation. Many different

Abbreviations: cryoEM, single particle cryo electron microscopy; AWI, air–water interface; ADP, adenosine diphosphate; ATP, adenosine triphosphate; DDM, n-Dodecyl-Beta-Maltoside; CMC, critical micelle concentration; CDA, cyclic di-AMP.

* Corresponding authors.
E-mail addresses: michele.darrow@rfi.ac.uk (M.C. Darrow), s.p.muench@leeds.ac.uk (S.P. Muench).
[1] Present address: Thermo Fisher Scientific, 168 Third Avenue, Waltham, MA USA 02451.

https://doi.org/10.1016/j.jsb.2025.108206
Received 28 October 2024; Received in revised form 10 March 2025; Accepted 28 April 2025
Available online 3 May 2025

approaches for mitigating the effects of AWI have been investigated, all of which are effective to various extents for different samples, though none providing a universal, surefire solution. Some of the most popular and effective approaches to mitigating AWI interactions are; (1) The addition of detergent at or just below its critical micelle concentration (CMC) to change the AWI properties and reduce likelihood of protein interaction with the AWI, (2) the use of grids with a continuous support film to sequester protein particles away from the AWI, (3) reducing the time available for AWI interactions by reducing the time between sample deposition on the grid and vitrification (hereafter referred to as plunge time) and (4) cross-linking between subunits in a complex. The correct approach to tackle AWI interactions for a given sample is not clear, with each approach having its advantages and disadvantages that depend on sample properties as well as ease of use and accessibility (Liu and Wang, 2023; Han, 2023; Hirst, 2024).

Aside from sample damage, protein flexibility is another significant difficulty in cryoEM. Like AWI interactions, this can be responded to through alterations to sample preparation approach, for example through the addition of stabilising mutations, crosslinks or ligands (Zhang, 2022; Kastner, 2008; Zhang et al., 2022). Flexibility can alternatively (or additionally) be addressed computationally during image processing using a variety of approaches. For proteins with symmetry, this can be exploited, using symmetry expansion followed by focused classification on the flexible region. There are also numerous algorithms for modelling flexibility such as 3D variability analysis and non-uniform refinement in cryoSPARC (Punjani et al., 2020; Punjani and Fleet, 2021) and multi-body refinement in RELION (Nakane, 2018), as well as neural network approaches to model continuous heterogeneity such as cryoDRGN (Zhong, 2021), Flex3D in cryoSPARC (Punjani and Fleet, 2023) and DynaMight in RELION (Schwab, 2024). Whilst the biochemical responses can be effective, straightforward solutions, one downside is that they involve structurally altering the sample, which could result in biologically irrelevant conformations. Addition of a ligand, for example, can result in resolving a different conformation to the conformation of interest. Alternatively, instead of trying to reduce or remove flexibility in the sample, the computational approaches listed above can be used to process data and produce a consensus map despite flexibility, however often at worse resolution. As protein flexibility is inherent to the function of most proteins, keeping the flexibility in the system and resolving it computationally is the most informative approach, but it is not always feasible to reveal the desired information at the required resolution.

In this paper, we investigate the challenges faced in pursuit of a high-resolution structure of the soluble, membrane-associated regulatory subunit of the KtrAB potassium transporter from *Bacillus subtilis,* KtrA. This 198 kDa protein appears at first glance to be an ideal specimen for cryoEM analysis. The biochemistry of KtrA is well established, it crystallises well and the crystal structure of ADP- and ATP-bound KtrA have been previously solved, although the apo structure has not (Vieira-Pires et al., 2013). The ligand-bound structures show that the monomers of this octameric protein have two domains – the amino (N)-lobe and the carboxy (C)-lobe, which come together to form dimers. Four of these dimers then tetramerise to form an octamer with the N-lobes forming a core ring and the C-lobes forming four protrusions from the core (Fig. 1). The ADP-bound octamer displays a diamond shaped ring structure with 2-fold symmetry. Structural studies (Chiang, 2024; Diskowski, 2017) reveal that KtrA.ADP inhibits K^+ ion transport by inducing a conformation of KtrB that has a loop with positive charge blocking the ion channel. When KtrA is in its stable, square-shaped ATP-bound conformation (which also requires bound Na^+) it induces a KtrB conformation in which the ion channel is no longer blocked, allowing movement of K^+ ions across the membrane through KtrB into the cell.

Despite the apparent suitability of KtrA for structure determination by cryoEM, initial attempts to solve the ADP-bound cryoEM structure using a standard approach (sample applied to 1.2/1.3 holey carbon grids vitrified using a Vitrobot, data collected using a Falcon4 detector in a 300 keV Krios microscope and processed using a standard pipeline in RELION 4 and later in CryoSPARC) produced data suffering from preferred orientation, missing density for the C-lobes, poor density for the rest of the map and a global resolution of 4 Å. Likewise, in the recent cryoEM structures of ATP- and ADP-bound KtrA in complex with the membrane spanning subunit of the transporter, KtrB, the C-lobes of KtrA are not well resolved (Chiang, 2024).

The challenges associated with determining the whole structure of KtrA by cryoEM, particularly when it is not in complex with KtrB, makes it an intriguing test specimen for investigations into whether, and how, different elements of the grid preparation process influence data quality and to what extent changes to grid preparation approach can overcome such difficulties. As protein interaction with the AWI during cryoEM grid preparation can cause or exacerbate issues such as preferred orientation (Klebl, 2020; Noble, 2018) and in some cases lead to protein denaturation and subunit dissociation (Glaeser, 2018; Lyumkis, 2019), some of the changes made to grid preparation approach were made with the aim of minimising AWI interactions. These were the reduction of plunge time and the addition of DDM as a surfactant. To achieve shorter plunge times, the chameleon® was used as a vitrification device instead of the Vitrobot. This means that as well as reducing plunge time for these experiments, the sample was also thinned by self-wicking grids, removing the blotting step and the potential for detrimental interactions with the

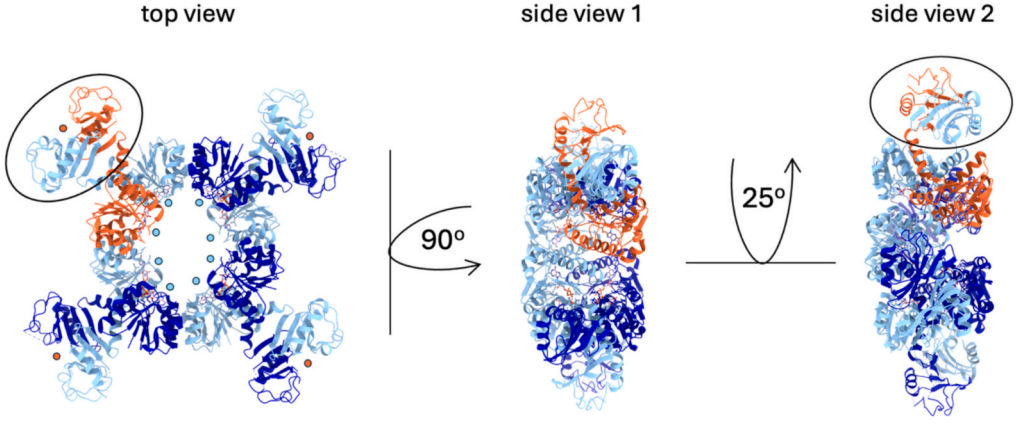

Fig. 1. Crystal structure of KtrA.ADP (PDB ID: 4J91; https://doi.org/10.2210/pdb4J91/pdb). The stoichiometry is a tetramer of dimers. In the top left dimer one monomer is coloured orange, otherwise, the alternating monomers are coloured dark and light blue. The C-terminal region of each dimer protrudes from the core ring and forms the C-lobes (black circle). There are four CDA binding sites, one in each C-lobe (orange circles). There are eight ATP/ADP binding sites, one in the N terminal domain of each monomer (light blue circles). The three views depicted are the views shown in the 2D classes in subsequent figures. (For interpretation of the references to colour in this figure legend, the reader is referred to the web version of this article.)

filter paper that have also been previously discussed as a potential problem during grid preparation (Lyumkis, 2019). As missing density can often be caused by flexibility (Suder and Gonen, 2024), and in our first reconstruction the C-lobe density was missing, addition of a ligand known to bind the C-lobes of KtrA, cyclic di-AMP (CDA) (Mudgal, 2021; Rocha, 2024) was explored to potentially stabilise these regions and improve the density. (Lyumkis, 2019).

To unpick the effects of the AWI (preferred orientation and denaturation/dissociation), and protein flexibility on the sample preparation process, a detailed study of single and double modifications to the sample preparation approach was used with KtrA as a case study.

2. Materials and Methods

2.1. KtrA expression and purification

KtrA was expressed, and in the final step purified in the same buffer as used for KtrA crystallisation (50 mM Tris pH 8.0, 150 mM KCL, 1 mM TCEP) as described in (Vieira-Pires et al., 2013; Chiang, 2024), with bound ADP maintained in the sample throughout purification. The sample was stored at −80°C. KtrA was then thawed on ice and diluted in Buffer A (without TCEP) to the desired concentration for grid preparation.

2.1.1. Mass Spectrometry analysis

To confirm correct expression of full-length KtrA (Uniprot ID: O32080), the intact mass of the expressed KtrA was determined by liquid chromatography mass spectrometry (LC-MS). Protein desalting and mass analysis was performed by LC-MS using an M−class ACQUITY UPLC (Waters UK, Manchester, UK) interfaced to a Xevo QToF G2-XS mass spectrometer (Waters UK, Manchester, UK). KtrA was diluted to 1 μM with 0.1 % TFA 99.9 % H_20. 1 μL of the 1 μM sample was injected onto an Acquity UPLC Protein BEH C4 column (300 Å, 1.7 μm, 2.1 mm × 100 mm, Waters UK) with an Acquity UPLC Protein BEH VanGuard Pre-Column (300 Å, 1.7 μm, 2.1 mm × 5 mm, Waters UK). Solvent A was 0.1 % formic acid in water, and solvent B was 0.1 % formic acid in AcN (v/v basis). System flowrate was kept constant at 50 μl/min. Protein sample was loaded on to the trap column in 20 % acetonitrile/0.1 % formic acid and washed for 5 min. Following valve switching, the bound protein was eluted by a gradient of 20–95 % solvent B in solvent A over 10 min. The column was subsequently washed with 95 % solvent B in A for 5 min before re-equilibration at 20 % solvent B in A ready for the next injection. The mass spectrometer was calibrated using a separate injection of glu-fibrinopeptide. Data were processed using MassLynx 4.2.

2.1.2. Additional ligands and surfactants

The minimum theoretical CDA:KtrA molar ratio required for full occupancy of CDA binding sites was calculated to be 20:1 using the protein–ligand binding web app developed by the Jiang lab at Purdue University (Jiang, 2023). Using this concentration as the minimum, CDA was added to KtrA in a molar ratio of 50:1 ligand:protein for the chameleon grids and 100:1 M ratio for the Vitrobot grids and incubated on ice for an hour before grid preparation. DDM was added at 0.00087 % DDM (1/10 of the CMC) immediately before grid preparation.

2.1.3. Grid preparation using the Vitrobot Mark IV (Thermo Fisher Scientific)

The KtrA concentration used was 0.5 mg/mL. Grids were glow discharged in air using the PELCO easiGlow for 30 s at 12 mA then 4 μL sample was applied to Quantifoil R 1.2/1.3 Cu 300 grids in a Vitrobot Mark IV (Thermo Fisher Scientific) and blotted for 6 s, blot force 6 before vitrification in liquid ethane.

2.1.4. Grid preparation using the chameleon (SPT Labtech).

KtrA concentration for all chameleon samples was 8 mg/mL. Quantifoil Active grids were glow discharged in air at 12 mA in the chameleon for 15 – 70 s to obtain an appropriate wicking rate for the desired dispense-to-plunge time. 6 nL sample was applied to the grid which was vitrified in liquid ethane after a plunge time of 54 to 2500 ms.

2.1.5. Single particle data collection and processing

Data were collected on a Titan Krios microscope operating at 300 keV with a Falcon IV/Falcon IVi direct electron detector (Thermo Fisher Scientific) operating in counting mode. For some datasets a Selectris energy filter was also used (see Sup. Table 1). EPU data acquisition parameters can be found in Sup. Table 1.

Data was pre-processed in RELION 4 using RELION's own implementation for motion correction and CTFFIND-4.1 for CTF estimation, particles were picked using crYOLO 1.8. 2D classification, and heterogeneous and non-uniform refinement, were performed using cryoSPARC v4. 2D classification was performed using circular masks with diameter of at least 200 Å and the masks used for non-uniform refinement were all generated during the refinement using the same 'dynamic masking' parameters in cryoSPARC. Further details of the processing pipeline for each dataset can be found in Sup. Fig. S1 and Sup. Table S2.

3. Results

After initial unsuccessful attempts in 2019 to obtain a high-resolution structure of KtrA by single particle cryoEM, we wished to re-examine our approach and better understand the reasons behind its intractability. In recent years, the percentage of datasets submitted to the EMDB at a resolution of 4 Å or better has increased from 48.5 % in 2019 to 73.4 % in 2023. This is due to improvements in both hardware and software, such as the superior electron counting capabilities of the Falcon 4 detector, the ability to store this information in Electron Event Representation (EER) files (Guo, 2020) and the accompanying response from data processing suites such as RELION in the form of motion correction using the Bayesian polishing algorithm (Zivanov et al., 2019). Given that the initial attempt at KtrA structure determination in 2019 was prior to these and other developments, we first followed the same sample preparation approach (using conventional blotting) to determine whether the latest data acquisition and processing pipelines could provide sufficient improvement in data quality to obtain a high-resolution structure.

Blotted holey carbon/copper grids were produced by use of a Vitrobot. Screening of these grids showed a sample with good mono dispersity and particle number per grid (Sup. Fig. 2). However, it became clear from 2D analysis that despite secondary structure within the core, the C-lobes were absent (Fig. 2A). 2D classification also indicated the presence of preferred orientation resulting in two specific 'side' views making up the majority of the 2D classes (Sup. Fig. 3A) and only 5 % of the particles showing 'top' views (Fig. 2A). This was confirmed by the viewing direction distribution (Fig. 2B) that also showed preferred orientation.

Heterogeneous and non-uniform refinement in cryoSPARC showed weak density for part of one of the C-lobe regions and the resolution of the core ring of KtrA was limited to 3.8 Å (Fig. 2C) Rigid body fitting of the KtrA.ADP monomer model from the KtrA.ADP crystal structure 4J91 confirmed that although the C-lobe density is missing, the rest of the complex is present and had the same monomer conformation as the crystal structure model (Fig. 2D). The global shape of the octamer core in our density map differs slightly from the global shape of the KtrA.ADP crystal structure hence why each monomer model from 4J91 was fitted individually as opposed to the whole biological assembly. This slight difference in monomer position within the octamer between the crystal structure and our EM density map is likely due to the effect of crystal contacts on the shape of the octamer. This is supported by a recently published cryoEM structure of KtrAB in which the octameric structure of KtrA also differs from the crystal structure and more closely resembles the ring shape of the density maps from our data (Chiang, 2024).

The sample was analysed by mass spectrometry and negative-stain

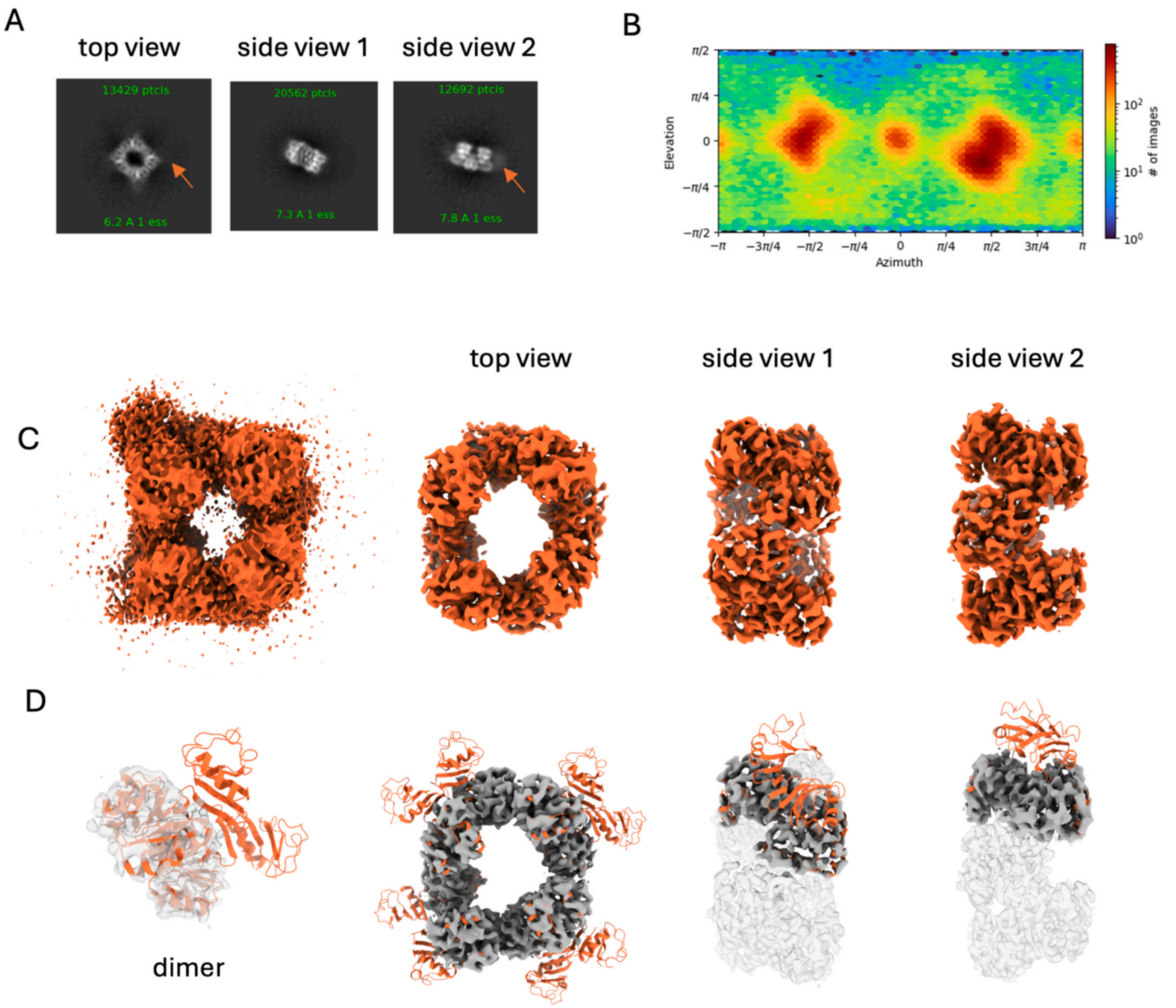

Fig. 2. CryoEM results from grids prepared using a conventional blotting approach. A) 2D classes of the most populated views, despite secondary structure visible in the core, density for the C-lobes is absent (orange arrows). B) Viewing direction distribution shows there is preferred orientation. C) 3D density map from non-uniform refinement. D) Rigid fit of monomer model from PDB: 4J91 (KtrA.ADP) shows the missing density for the C-lobes. (For interpretation of the references to colour in this figure legend, the reader is referred to the web version of this article.)

EM with both showing the protein sample was pure and intact (Sup. Figs. 4 & 5). Therefore, it appeared likely that either flexibility or degradation of the protein due to the harsh environment in the thin film during grid preparation, or a combination of both were the cause of the poor quality of our initial dataset. To establish which problems were causing the poor quality and attempt to overcome them, a methodical approach was used to assess the effects of single and double modifications to sample preparation as compared to the baseline blotted grid (Table 1). For each sample, the imaging and processing protocols were kept as consistent as possible whilst still ensuring the data was processed optimally for the variable characteristics it displayed (Sup. Fig. 1).

Reduced plunge time and no blotting: Studies by us and others (Klebl, 2020; Levitz, 2022; Gardner, 2023) have shown that improvements in particle orientation and reduced denaturation and dissociation of subunits can be achieved through a much shorter plunge time (typically milliseconds vs seconds), which also involves the removal of blotting. To test if the absence of density for the C-lobes and the preferred orientation observed with the baseline (Vitrobot, 6 s; Fig. 2)

Table 1
Modifications made to conventional sample preparation approach for each dataset. A set of single modifications were made initially before double modifications were selected based on these results.

Modifications	Freezing Device	Plunge Time	Additive
Baseline	Vitrobot	6 s	none
Single	chameleon	54 ms	none
Single	chameleon	100 ms	none
Single	chameleon	300 ms	none
Single	chameleon	2500 ms	none
Single	Vitrobot	6 s	DDM (surfactant)
Single	Vitrobot	6 s	CDA (ligand)
Double	chameleon	180 ms	DDM (surfactant)
Double	chameleon	2500 ms	DDM (surfactant)
Double	chameleon	100 ms	CDA (ligand)

were due to AWI interactions or interactions with blotting paper during grid making, we used the chameleon system and associated self-wicking grids to prepare grids of KtrA with 54 ms, 100 ms, 300 ms and 2500 ms plunge times (Fig. 3B-E).

In agreement with previous reports (Klebl, 2020; Levitz, 2022; Gardner, 2023), screening of these grids showed that the particle concentration for the 54 ms plunge time was considerably lower (an average of 16 particles per micrograph) than for the grids made with longer plunge times (these ranged from 176 to 350 particles per micrograph, dependent on plunge time) despite the concentration of sample remaining consistent across all plunge times (8 mg/mL). This significantly higher concentration is required for short plunge times on the chameleon due to the previously observed (Levitz, 2022; Levitz, 2022) lack of any concentrating effect of particles when grids are prepared using highspeed droplet dispensing systems as opposed to blot-based approaches and the potential for particles to cluster in the droplets during flight and end up in ice too thick to image as proposed by Klebl et al (Klebl, 2020). Although a slightly lower (but still higher than 0.5 mg/mL) concentration, such as 2 or 3 mg/mL, would have been usable for the longer chameleon plunge time (2500 ms), 8 mg/mL was used for all chameleon grids to minimise variability between conditions.

The 2D classes showed clear differences between the datasets but are limited in their analysis as the contrast of the signal strength between the lobes with different mobility is harder to discern. Therefore, these datasets were processed to 3D refinement at which point the size of the particle stacks were normalised to the smallest stack (35,383 particles) before reconstruction to a 3D volume. The volumes were then low pass filtered to the poorest resolution (8 Å) and visualised in ChimeraX. This allowed us to compare the apparent strength of the lobe density to that of the core through contouring of the map. We used the map statistics

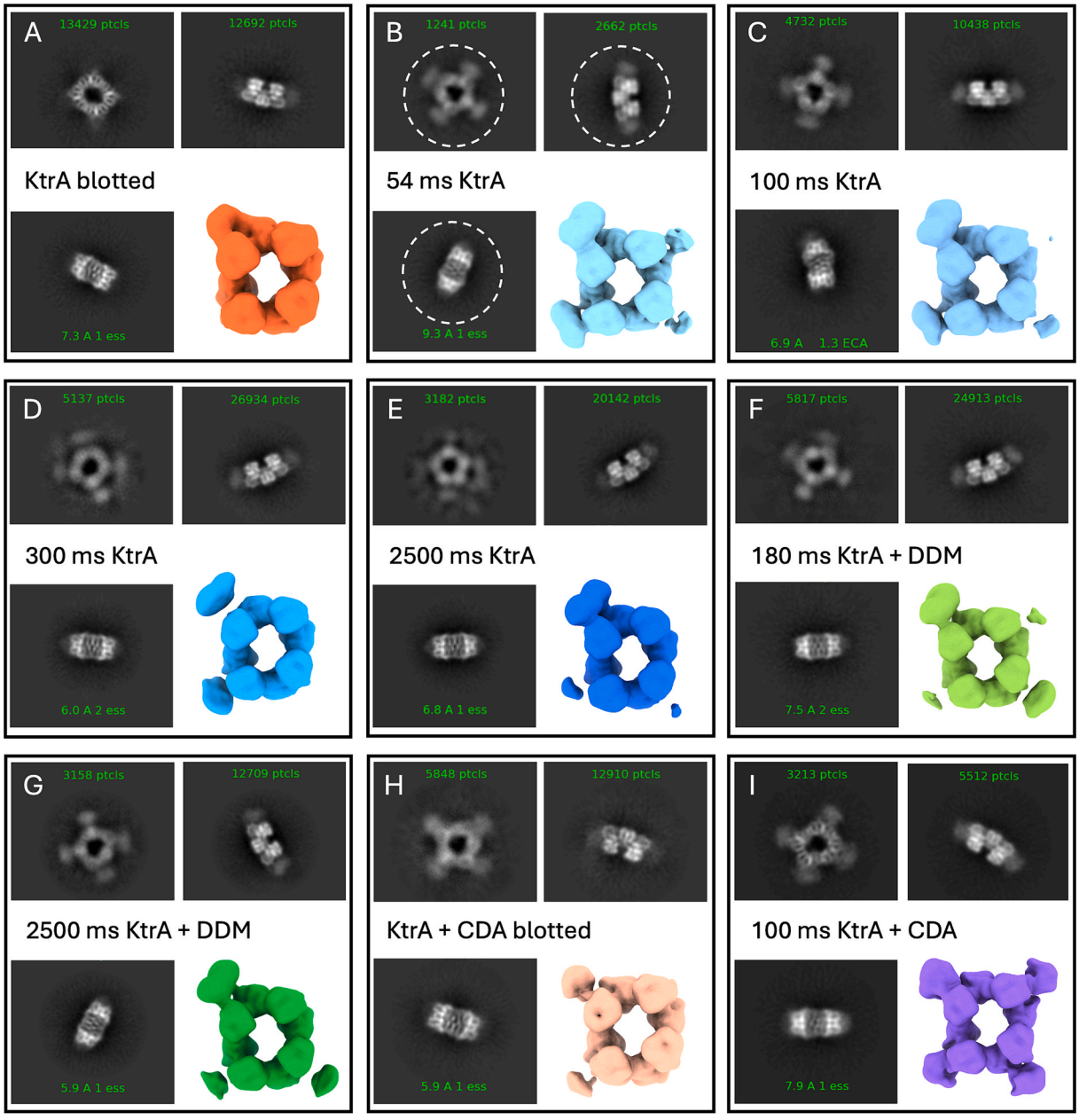

Fig. 3. 2D classes and 3D density maps for each sample preparation approach. 2D classes of the same three views depicted in Figs. 1 and 2 are shown here for each sample preparation condition. A circular mask of at least 200 Å was used for class2D (highlighted with a white dotted circle in B). For each dataset, the top left class is the top view, the bottom left class is side view 1 and the top right class is side view 2. The resultant 3D density map for each condition is also shown. Each map is from a non-uniform refine of 35,383 particles. The resulting maps were low pass filtered to 8 Å and visualised in ChimeraX with a normalised threshold.

tool in ChimeraX to represent the maps at a normalised contour threshold to compare the strength of the lobe density as shown in Fig. 3.

The resultant 2D classes suggested a significant improvement in the integrity of the C-lobes compared to the Vitrobot sample for all plunge times but particularly for the 54 ms dataset (Fig. 3). It is notable that the signal for the core is stronger in the 2D class of the top view from the blotted dataset than in the short chameleon plunge time datasets. This is likely due to the absence of the C-lobe density in this dataset allowing more accurate angular assignments for the remaining core. The 3D reconstructions also showed an improvement in C-lobe density, however this part of the map was still lower resolution than the core for all datasets and none of the maps had density for all four C-lobes. The blurriness of the density for the C-lobes in the 54 ms, 100 ms and 300 ms plunge time 2D classes, compared to the core density, suggests these regions are flexible.

In all the KtrA datasets, the top view is a limited view, and this view becomes more limited the longer the plunge time on the chameleon (Fig. 3B-E & 4A). The viewing direction distributions also show an increase in preferred orientation with the chameleon plunge times longer than 100 ms (Fig. 5B-E). This is particularly apparent for the 2500 ms plunge time for which the preferred orientation results in clear anisotropy in the map and only a single blurry class of top views in 2D classification (Fig. 3E) (Sup. Video 1). Interestingly, the preferred orientation in the 2500 ms dataset is worse than in the 6 s blotted dataset despite the time available for AWI interactions being less than half.

The improvements in C-lobe density and angular distribution seen for the ≤300 ms plunge time chameleon grids compared with the Vitrobot dataset as well as the increase in preferred orientation and the reduction in the density for the C-lobes when the chameleon plunge time is 2500 ms, suggest that AWI interactions during grid preparation are a cause of the missing C-lobe density and preferred orientation. Despite the improvements seen when the chameleon is used to reduce the plunge time, the C-lobe density is still weaker than the density for the rest of the protein, even for the shortest plunge time (Fig. 3B). Reducing plunge time is one of several ways in which preferred orientation can be mitigated; two other ways are collecting tilted datasets and the use of a continuous support film. The advantage of these approaches is that they do not require expensive, specialist sample preparation equipment. However, neither are they silver bullets – in this case, collecting tilted datasets on the 54 ms and 100 ms grids did not further improve angular distribution (data not shown) so this approach was not pursued further. Additionally, the use of a continuous support film (graphene oxide) resulted in a considerable increase in preferred orientation, producing a dataset containing only top views (Sup. Fig. 6).

DDM as a surfactant: Given that the impacts of AWI interactions can be mitigated by reducing plunge time, grids were prepared with the surfactant DDM with both a short (180 ms) and a long (2500 ms) plunge time on the chameleon to establish whether this could further reduce the impacts of the AWI. To provide a comparison to the initial Vitrobot baseline, a sample + DDM was also prepared on the Vitrobot but this resulted in aggregation too severe for data collection (Sup. Fig. 7). The 180 ms and 2500 ms chameleon datasets with DDM added (Fig. 3F & G) did not display aggregation and the 2500 ms dataset showed a slight improvement in C-lobe density compared with the chameleon dataset of the same plunge time without DDM (Fig. 3E & 3G, 2D classes and 3D map). As DDM was being used here to probe the effects of altering AWI interactions in relation to plunge time, other detergents were not screened despite the aggregation seen with the Vitrobot. The number of readily available detergents makes screening these a study in and of itself; a good example of this which explores the effect of various detergents on preferred orientation, in particular in relation to surface charge, was published recently (Yadav and Vinothkumar, 2024). Applying this systematic approach to screening a range of detergents and concentrations would likely identify a detergent concentration and type that is amenable to KtrA on the Vitrobot.

In the case of the 2500 ms datasets, DDM resulted in an improvement in angular distribution, increasing the proportion of top views and reducing the anisotropy of the 3D reconstruction (Fig. 4, Sup. Video 1). These results show that adding DDM mitigated the increase in preferred orientation seen in the 2500 ms plunge time dataset compared with a ≤100 ms plunge time. However, DDM did not have an additional effect on angular distribution or C-lobe density when the plunge time was already short (180 ms).

Addressing flexibility with CDA: The above results show that AWI interactions have a strong influence on preferred orientation and the C-lobe density observed in the cryoEM maps, and that minimisation of AWI interactions using a short plunge time or addition of DDM reduces these effects. However, the density for the C-lobes is still weaker than the density for the core ring of KtrA. Another cause of missing density in a cryoEM map can be inherent flexibility of that region resulting in blurring of the signal during averaging. To address this possibility, CDA, a ligand that binds the C-lobes (Kim, 2015), was added to explore whether this would increase C-lobe stability enough for them to be resolved. Kim *et al* used X-ray crystallography to solve the structure of one C-lobe from *S. aureus* in complex with CDA (PDB 4XTT). This structure shows CDA bound at the interface between the two monomers and that the monomers are closer together than in structures without CDA (Kim, 2015).

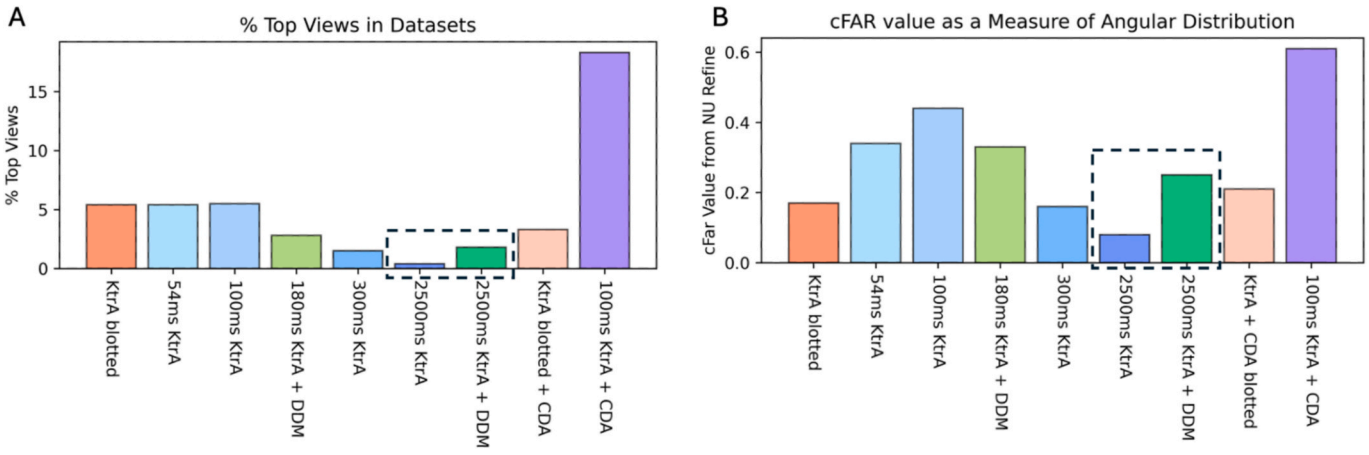

Fig. 4. Quantification of angular distribution. The addition of DDM for the 2500 ms dataset results in a marked improvement in angular distribution compared to the same plunge time without DDM (dashed box). Addition of CDA has little impact on angular distribution for the blotted dataset but results in a dramatic improvement for the 100 ms dataset. A) The percentage of top views (a limited view) in each dataset in the final round of class2D. B) The numerical measure of angular distribution calculated by cryoSPARC in the final non-uniform refinement for each dataset.

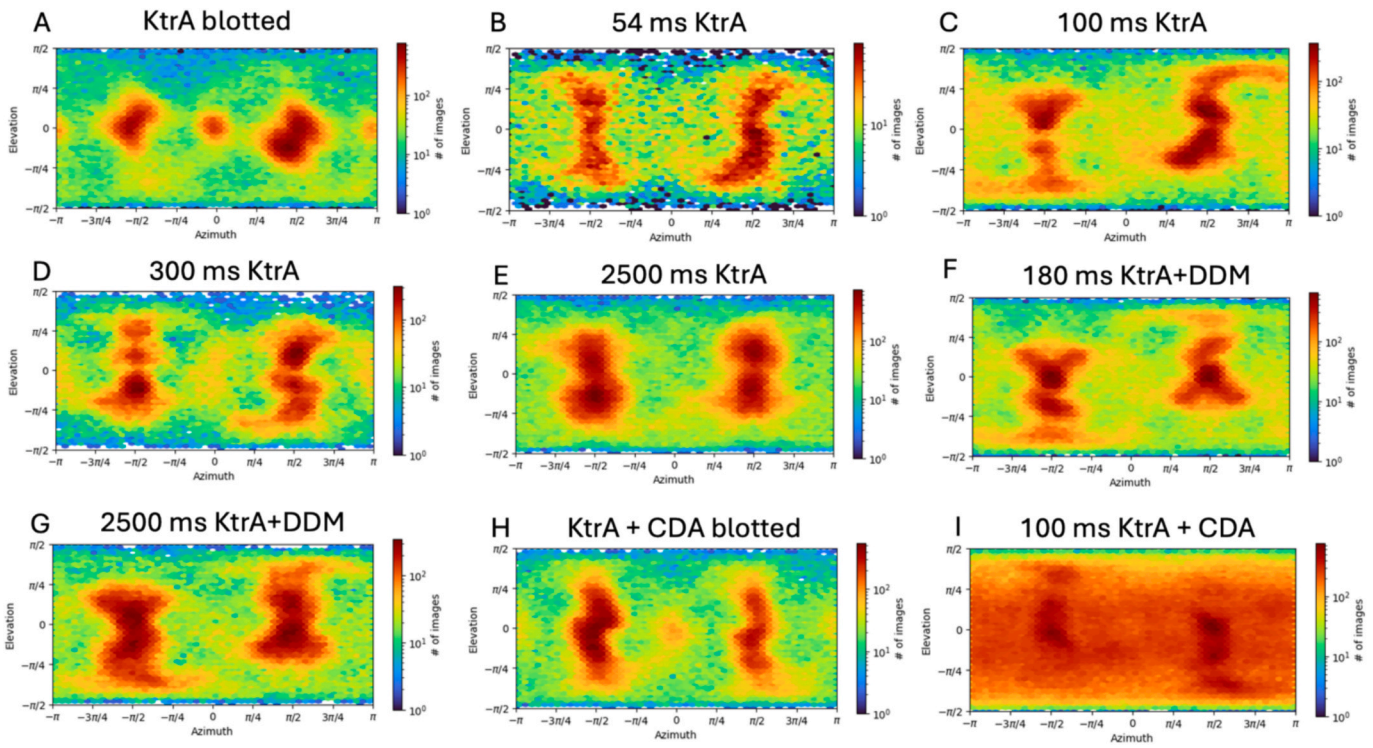

Fig. 5. Viewing direction distributions for each sample preparation approach as calculated by cryoSPARC. The combination of a 100 ms plunge time with the addition of CDA leads to the most significant improvement in angular distribution.

KtrA + CDA prepared on the Vitrobot had significantly better density for the C-lobes in the 2D classes compared to the original blotted sample, but the 3D reconstruction only showed a marginal improvement (Fig. 3A & H). There was also a marginal improvement in angular distribution (Fig. 4B, Fig. 5A & H). Given that addressing AWI interactions showed improvements in these areas, KtrA + CDA was prepared on the chameleon with a 100 ms plunge time. These conditions resulted in the biggest improvement in C-lobe density, with all four lobes present (Fig. 3I), and a significant improvement in angular distribution (Figs. 4 & 5I). Additionally, resolution of the C-lobes was sufficient to show that the conformation of the C-lobes in the 100 ms KtrA + CDA density map is different to that in the 100 ms KtrA map (Fig. 3C & 3I, Sup. Fig. 8, Sup. Video 2) even though C-lobe resolution was still worse than the resolution of the core (Sup. Fig. 9). The C-lobes in the 100 ms KtrA + CDA map are narrower, consistent with the observation from the truncated C-lobe crystal structure from *S. aureus* that showed that the monomers move closer together when CDA is bound (Kim, 2015) and this crystal structure fits well into the C-lobe of the 100 ms KtrA + CDA density map (Sup. Video 3). Note that for docking of the CDA-bound C-lobe structure we removed residues 133 to 139 as these residues form the helix that connects the C-lobes to the core of KtrA based on the ADP-bound crystal structure PDB 4J91, but in the truncated form these helices fold back on the structure, likely due to the truncation.

4. Discussion

KtrA suffers from preferred orientation and missing C-lobe density when grids are prepared using a standard blotting approach. Reducing the time of grid preparation with shorter plunge times improves the C-lobe density and the improvement is the most significant with the shortest plunge times: 54 ms and 100 ms. As the plunge time on the chameleon increases across the ranges used in this study (54 ms to 2500 ms) the preferred orientation becomes worse and the C-lobe density decreases, resulting in the dataset from the 2500 ms plunge time having almost no top views, the lowest cFAR value, and density for only one C-lobe, as opposed to the 54 ms dataset which has some density for all 4 lobes, one of the highest cFAR values and >5 % of particles are top views. Addition of DDM at 0.1x CMC when a 2500 ms plunge time is used mitigates these effects on angular distribution and restores the preferred orientation to levels similar to the 100–300 ms plunge time datasets. The improved angular distribution of the shorter (54 ms and 100 ms) plunge times and the 2500 ms + DDM dataset compared to the 2500 ms plunge time without DDM show that AWI interactions over a millisecond to second timescale contribute to preferred orientation due to reduction of the time available for AWI interactions or alteration of chemical properties of the AWI with DDM resulting in reduced preferred orientation. These findings fit well with the model for AWI interaction proposed by Klebl et al in figure 7 of (Klebl, 2020) where they propose that initial contact with the AWI happens in ≤1 ms but that partial denaturation and unfolding occurs on a ms – s timescale. Interestingly, preferred orientation is worse in the 2500 ms dataset without DDM than in the 6 s blotted dataset (Fig. 4, Sup. Fig. 3A & 3E) despite the much longer plunge time in the blotted 6 s dataset. This shows that although increasing the time available for AWI interactions within the same grid preparation system (from 54 ms to 2500 ms on the chameleon) increases preferred orientation, time is not the only factor at play because in a system that uses blotting, a plunge time as long as 6 s results in data with a better angular distribution than 2500 ms without blotting for this sample. Armstrong et al (Armstrong, 2020) highlighted some of the other factors affecting the sample during blotting such as the irregular pattern of fibres in the filter paper causing pockets of air to form and propagate, resulting in uneven dewetting of the grid and the exposure of the sample to shear stresses. The fluidics happening during sample application with the chameleon will likely be as complex although the exact processes will be different.

Taken together, these results show that AWI interactions are a cause of C-lobe loss and preferred orientation and that these effects take place on a millisecond to second timescale despite the fact that the majority of particles are already associated with the AWI in the 100 ms dataset (tomography data not shown). The improvements in angular

distribution seen when a 2500 ms plunge time is used with DDM, rather than without, show that addition of a surfactant can protect against these longer timescale processes almost as effectively as reducing the plunge time to 100 ms. Despite this, the lack of improvement in angular distribution for the 180 ms DDM dataset compared to the 100 ms dataset shows that addition of DDM does not result in additional improvements on top of those already seen when a fast (<300 ms) plunge time is used for this sample.

As a higher protein concentration is required for faster plunge times, the observation that a 2500 ms plunge time with DDM can protect from the negative effects of the AWI on angular distribution almost as effectively as a 100 ms plunge time is useful for samples that need the protection of a short plunge time, but which are difficult or impossible to prepare in high concentrations. For these samples, the use of a longer plunge time in the presence of DDM may be just as effective.

Contrastingly to DDM, addition of CDA does lead to improvements additional to those seen when a 100 ms plunge time on the chameleon is used, likely because in this case the two modifications are addressing different issues: CDA is primarily addressing flexibility and the 100 ms plunge time is addressing AWI interactions.

The initial aim of this study was to develop a robust pipeline to permit the structure determination of KtrA with a variety of ligands. However, we found that despite a range of different approaches, the KtrA-ADP- CDA complex was the most amenable, and as there is currently no CDA-bound full length structure of KtrA, this provides new structural detail on this important complex. However, in other cases, adding a ligand to increase tractability of a sample is not a viable solution because it changes the biological question being answered.

The sample preparation approaches explored in this study show that the issues faced arise from multiple different sources, namely damage to the sample in the thin film environment and flexibility, both resulting in missing density for the C-lobes. Changes made to sample preparation approach to reduce exposure to the AWI through reducing the plunge time improved the density for the C-lobes but it was still incomplete. Adding a ligand that binds the C-lobes, CDA, resulted in slightly improved density for the C-lobes when grids were prepared with a 6 s plunge time on the Vitrobot. When grids of KtrA + CDA were prepared on the chameleon with a 100 ms plunge time, this resulted in much better density for the C-lobes and a significant improvement in angular distribution.

The improvement in C-lobe density is likely due in part to the reduced flexibility of the more compact CDA-bound conformation. But the marked improvement in C-lobe density in the 100 ms KtrA + CDA dataset compared to the blotted KtrA + CDA dataset show that addressing flexibility alone is not sufficient to obtain this observed improvement in C-lobe density and that reduced exposure to the AWI is also required. Likewise, the striking improvement in angular distribution in the 100 ms KtrA + CDA dataset compared to the other datasets including the blotted KtrA + CDA dataset also suggests that binding of CDA alone is not the sole cause of these observed changes. The prevalence of side views in all the datasets and the weak density for the C-lobes suggest that KtrA could be associating to the AWI via the C-lobes. The C-lobes of KtrA + CDA have a different conformation and surface charge to the apo C-lobe conformation (Sup. Fig. 8 & 10) resulting in a slight increase in negative surface charge in the CDA-bound C-lobes (Sup. Fig. 10). If KtrA is associating with the AWI via its C-lobes, the KtrA.CDA C-lobe conformation and altered surface charge could make association with the AWI less favourable, particularly since there is a negative charge at the AWI and the CDA-bound C-lobes have more negative surface charge. The difference seen in the impact of CDA depending whether the grid was prepared with a 6 s blotted plunge time or with 100 ms plunge time suggests that this reduction in affinity of the C-lobes for the AWI mitigates the impacts of AWI interactions over a 100 ms timescale but that over a longer time period and/or the process of blotting, C-lobe damage and preferred orientation occurs in spite of the presence of CDA.

Another observation is that the samples prepared with DDM present showed density for alternate C-lobes whereas those without DDM always showed density for consecutive C-lobes. This suggests that there is a preferred way in which KtrA interacts with the AWI that changes when DDM is present resulting in a different pattern of C-lobe density loss.

Although the sample preparation approaches explored in this study shone light on some of the causes of complications for this sample and explored various ways of mitigating them, none of the approaches removed the complications entirely. C-lobe density could be improved significantly compared to the standard blotting approach, but it was not possible to obtain C-lobe density as strong as the density for the core. The improvements seen for C-lobe density when exposure to the AWI is reduced show that some of the loss of density was due to avoidable AWI exposure, and some is due to flexibility which can be reduced through the addition of a ligand, although neither approach fully resolved the issue. This work demonstrates the significant impact grid preparation can have on the quality and completeness of data collected and some of the ways in which these can be improved. Research into the effects of sample preparation on resultant data quality has already improved the accuracy and range of tools available for sample preparation optimisation. This study highlights the need for continued study and advances in this area so that our understanding is at a level that allows standardised approaches rather than the current roulette wheel approach to cryoEM sample preparation.

CRediT authorship contribution statement

Isobel Jackson Hirst: Writing – review & editing, Writing – original draft, Visualization, Methodology, Investigation, Formal analysis. **Wesley Tien Chiang:** Investigation. **Nien-Jen Hu:** Writing – review & editing. **Charlotte A. Scarff:** Writing – review & editing, Validation, Supervision, Project administration, Methodology, Conceptualization. **Rebecca F. Thompson:** Writing – review & editing, Validation, Supervision, Project administration, Methodology, Conceptualization. **Michele C. Darrow:** Writing – review & editing, Supervision, Resources, Project administration, Investigation, Funding acquisition, Conceptualization. **Stephen P. Muench:** Writing – review & editing, Supervision, Resources, Project administration, Investigation, Funding acquisition, Conceptualization.

Declaration of competing interest

The authors declare the following financial interests/personal relationships which may be considered as potential competing interests: [Michele Darrow is a former employee of SPT Labtech, manufacturers of the chameleon and self-wicking grid. Rebecca Thompson is a current employee of Thermo Fisher Scientific. The remaining authors declare that they have no known competing financial interests or personal relationships that could have appeared to influence the work reported in this paper].

Acknowledgements

Thank you to the Astbury Biostructure Laboratory at Leeds University for excellent support and for use of the Vitrobot and the Titan Krios microscopes as well as support from James Ault in the FBS mass spectrometry facility. Thank you to SPT Labtech Ltd, for the use of the chameleon. The Rosalind Franklin Institute is funded by UK Research and Innovation through the Engineering and Physical Sciences Research Council. Funding to support MCD was also provided by the Wellcome Trust through the Electrifying Life Science grant 220526/Z/20/Z. This work was funded by a Biotechnology and Biological Sciences Research Council (BBSRC) grant to S.P.M (BB/X007227/1). The Astbury Biostructure facility was funded through the University of Leeds and the Wellcome Trust (198466/Z/15/Z). C.A.S. is supported by a British Heart Foundation (BHF) Jacqueline Murray Coomber Fellowship (FS/20/21/

34704).

Data availability statement

EM maps were deposited to the Electron Microscopy Data Bank (EMDB). The EMDB accession codes are: EMD-51928 (blotted KtrA, full particle stack from Fig. 2). The rest are the 35383 particle stacks used from each dataset for comparison in Figs. 3-5. EMD-51919 (blotted KtrA), EMD-51920 (54 ms KtrA), EMD_51921 (100 ms KtrA), EMD_51922 (300 ms KtrA), EMD_51923 (2500 ms KtrA), EMD-51924 (blotted KtrA + CDA), EMD_51925 (180 ms KtrA + DDM), EMD_51926 (2500 ms KtrA + DDM), EMD-51927 (100 ms KtrA + CDA). (Sup. Table 3)

Appendix A. Supplementary data

Supplementary data to this article can be found online at https://doi.org/10.1016/j.jsb.2025.108206.

Data availability

Data is available in the EMDB depositions stated.

References

Mobbs, J.I., et al., 2021. *Structures of the human cholecystokinin 1 (CCK1) receptor bound to Gs and Gq mimetic proteins provide insight into mechanisms of G protein selectivity*. PLoS Biol 19 (6), e3001295.

Han, F., et al., 2023. *Structures of Tetrahymena thermophila respiratory megacomplexes on the tubular mitochondrial cristae*. Nat Commun 14 (1), 2542.

Weissenberger, G., Henderikx, R.J.M., Peters, P.J., 2021. *Understanding the invisible hands of sample preparation for cryo-EM*. Nat Methods 18 (5), 463–471.

Glaeser, R.M., 2021. *Preparing Better Samples for Cryo-Electron Microscopy: Biochemical Challenges Do Not End with Isolation and Purification*. Annu Rev Biochem 90, 451–474.

Punjani, A., Zhang, H., Fleet, D.J., 2020. *Non-uniform refinement: adaptive regularization improves single-particle cryo-EM reconstruction*. Nat Methods 17 (12), 1214–1221.

Yadav, S., Vinothkumar, K.R., 2024. *Factors affecting macromolecule orientations in thin films formed in cryo-EM*. Acta Crystallogr D Struct Biol 80 (Pt 7), 535–550.

Chen, S., et al., 2022. *Interaction of human erythrocyte catalase with air-water interface in cryoEM*. Microscopy (oxf) 71 (Supplement_1), i51–i59.

D'Imprima, E., Kuhlbrandt, W., 2021. *Current limitations to high-resolution structure determination by single-particle cryoEM*. Q Rev Biophys 54, e4.

Glaeser, R.M., 2018. *Proteins, Interfaces, and Cryo-Em Grids*. Curr Opin Colloid Interface Sci 34, 1–8.

Glaeser, R.M., Han, B.G., 2017. *Opinion: hazards faced by macromolecules when confined to thin aqueous films*. Biophys Rep 3 (1), 1–7.

Klebl, D.P., et al., 2020. *Need for Speed: Examining Protein Behavior during CryoEM Grid Preparation at Different Timescales*. Structure 28 (11), 1238–1248 e4.

Klebl, D.P., et al., 2022. *It started with a Cys: Spontaneous cysteine modification during cryo-EM grid preparation*. Front Mol Biosci 9, 945772.

Levitz, T.S., et al., 2022. *Effects of chameleon dispense-to-plunge speed on particle concentration, complex formation, and final resolution: A case study using the Neisseria gonorrhoeae ribonucleotide reductase inactive complex*. J Struct Biol 214 (1), 107825.

Noble, A.J., et al., 2018. *Routine single particle CryoEM sample and grid characterization by tomography*. Elife 7.

Liu, N., Wang, H.W., 2023. *Better Cryo-EM Specimen Preparation: How to Deal with the Air-Water Interface?* J Mol Biol 435 (9), 167926.

Han, B.G., et al., 2023. *Challenges in making ideal cryo-EM samples*. Curr Opin Struct Biol 81, 102646.

Hirst, I.J., et al., 2024. *CryoEM grid preparation: a closer look at advancements and impact of preparation mode and new approaches*. Biochem Soc Trans 52 (3), 1529–1537.

Zhang, K., et al., 2022. *Fusion protein strategies for cryo-EM study of G protein-coupled receptors*. Nat Commun 13 (1), 4366.

Kastner, B., et al., 2008. *GraFix: sample preparation for single-particle electron cryomicroscopy*. Nat Methods 5 (1), 53–55.

Zhang, K., Julius, D., Cheng, Y., 2022. *A step-by-step protocol for capturing conformational snapshots of ligand gated ion channels by single-particle cryo-EM*. STAR Protoc 3 (4), 101732.

Punjani, A., Fleet, D.J., 2021. *3D variability analysis: Resolving continuous flexibility and discrete heterogeneity from single particle cryo-EM*. J Struct Biol 213 (2), 107702.

Nakane, T., et al., 2018. *Characterisation of molecular motions in cryo-EM single-particle data by multi-body refinement in RELION*. Elife 7.

Zhong, E.D., et al., 2021. *CryoDRGN: reconstruction of heterogeneous cryo-EM structures using neural networks*. Nat Methods 18 (2), 176–185.

Punjani, A., Fleet, D.J., 2023. *3DFlex: determining structure and motion of flexible proteins from cryo-EM*. Nat Methods 20 (6), 860–870.

Schwab, J., et al., 2024. *DynaMight: estimating molecular motions with improved reconstruction from cryo-EM images*. Nat Methods 21, 1855–1862.

Vieira-Pires, R.S., Szollosi, A., Morais-Cabral, J.H., 2013. *The structure of the KtrAB potassium transporter*. Nature 496 (7445), 323–328.

Chiang, W.T., et al., 2024. *Structural basis and synergism of ATP and Na(+) activation in bacterial K(+) uptake system KtrAB*. Nat Commun 15 (1), 3850.

Diskowski, M., et al., 2017. *Helical jackknives control the gates of the double-pore K(+) uptake system KtrAB*. Elife 6.

Lyumkis, D., 2019. *Challenges and opportunities in cryo-EM single-particle analysis*. J Biol Chem 294 (13), 5181–5197.

Suder, D.S., Gonen, S., 2024. *Mitigating the Blurring Effect of CryoEM Averaging on a Flexible and Highly Symmetric Protein Complex through Sub-Particle Reconstruction*. Int J Mol Sci 25 (11).

Mudgal, S., et al., 2021. *Cyclic di-AMP: Small molecule with big roles in bacteria*. Microb Pathog 161 (Pt A), 105264.

Rocha, R., et al., 2024. *c-di-AMP determines the hierarchical organization of bacterial RCK proteins*. Proc Natl Acad Sci U.S.A 121 (18), e2318666121.

Jiang, W. *Protein-ligand binding web app*. 2023 [cited 2023 20/12/2023]; Available from: https://binding.streamlit.app/.

Guo, H., et al., 2020. *Electron-event representation data enable efficient cryoEM file storage with full preservation of spatial and temporal resolution*. IUCrJ 7 (Pt 5), 860–869.

Zivanov, J., Nakane, T., Scheres, S.H.W., 2019. *A Bayesian approach to beam-induced motion correction in cryo-EM single-particle analysis*. IUCrJ 6 (Pt 1), 5–17.

Gardner, S., et al., 2023. *Structural basis of substrate progression through the bacterial chaperonin cycle*. Proc Natl Acad Sci U.S.A 120 (50), e2308933120.

Levitz, T.S., et al., 2022. *Approaches to Using the Chameleon: Robust, Automated, Fast-Plunge cryoEM Specimen Preparation*. Front Mol Biosci 9, 903148.

Kim, H., et al., 2015. *Structural Studies of Potassium Transport Protein KtrA Regulator of Conductance of K+ (RCK) C Domain in Complex with Cyclic Diadenosine Monophosphate (c-di-AMP)*. J Biol Chem 290 (26), 16393–16402.

Armstrong, M., et al., 2020. *Microscale Fluid Behavior during Cryo-EM Sample Blotting*. Biophys J 118 (3), 708–719.